SPHERIC 2023

Rhodes, Greece, 27-29 June

Proceedings of the 17th International SPHERIC Workshop

Editor
Georgios Fourtakas

SPHERIC 2023

Proceedings of the 17th International SPHERIC Workshop

Rhodes Island, Greece, 27-29 June 2023

Organized by:
School of Engineering
Faculty of Science and Engineering
The University of Manchester
UK

Editor
Georgios Fourtakas

Published by The University of Manchester, UK
ISBN 978-1-3999-5885-1

Acknowledgements

The 17th International SPHERIC Workshop was supported by the School of Engineering, Faculty of Science and Engineering, The University of Manchester.

The local organising committee would like to acknowledge the help and support from our colleagues in the University of Manchester. We convey our deepest and sincere gratitude to the SPHERIC Scientific and Steering Committee for their guidance, advice and assistance, without them none of this would have ever been possible.

We would like to say a special thank you to Dr Aaron English for creating our SPHERIC 2023 logo and helping us with the organisation of the workshop.

Foreword

Dear Delegate,

Since its conception in 2005 with the Inaugural Meeting in Chatou, France, the Smoothed Particle Hydrodynamics rEsearch and Engineering International Community (SPHERIC) has foster, steered and disseminated the development and application of the Smoothed Particle Hydrodynamics (SPH) method in academia and industry alike.

The International SPHERIC Workshops are a unique series of yearly events with exclusive focus on the SPH method and associated particle-based methods. SPH has been widely adopted in the field of computational fluid mechanics, solid mechanics, geomechanics, manufacturing engineering and many other disciplines. The SPH scheme is considered to be the mainstream method for free-surface flows, and multi-phase flows, high non-linear deformation, fracture and fragmentation and, complex physics due to its meshless particle-based nature.

The SPHERIC workshop brings together state-of-the-art developments from academia and novel interdisciplinary applications from industry in a unique blend towards the advancement of the numerical scheme.

It is our pleasure and privilege to host the 17th edition of the International SPHERIC Workshop in Rhodes Island, Greece and I am looking forward to welcoming you for a stimulating and fruitful event.

Sincerely,

Georgios Fourtakas
Chair of the Local Organizing Committee
17th International SPHERIC Workshop

Committees

Scientific Committee

Prof. Renato Vacondio (Università di Parma, Italy)
Prof. Antonio Gil (Swansea University, UK)
Prof. Raj Das (RMIT University, Australia)
Prof. Ben Rogers (University of Manchester, UK)
Dr. Georgios Fourtakas (University of Manchester, UK)
Dr. Chun Hean Lee (Universiy of Glasgow, UK)
Prof Alex Crespo (Universidade de Vigo, Ourense, Spain)
Prof. Abbas Khayyer (Kyoto University, Japan)
Prof. David Le Touzé (Ecole Centrale de Nantes, France)
Dr Nathan Quinlan (National University of Ireland, Galway, Ireland)
Dr. Xiangyu Hu (Technical University of Munich, Germany)
Dr. Pengnan Sun (Sun Yat-sen University, China)
Dr. Tom De Vuyst (University of Hertfordshire, UK)
Dr Christopher Curtis Long (Los Alamos National Laboratory, USA)
Prof. Moncho Gómez-Gesteira (Universidade de Vigo, Spain)
Prof. Xu Fei (Northwestern Polytechnical University, China)
Dr. Rouhollah Fatehi (Persian Gulf University, Iran)
Dr. Nathaniel Albert Trask (Sandia National Laboratories, USA)
Prof. Mehmet Yildiz (Sabanci University, Turkey)
Prof. Andrea Colagrossi (CNR-INM, Italy)
Dr. Matthieu De Leffe (Siemens Digital Industries, France)
Dr. Salvatore Marrone (CNR-INM, Italy)
Prof. Peter Eberhard (University of Stuttgart, Germany)
Dr. Steven Lind (University of Manchester, UK)
Mr. Pierre Sabrowski (Dive Solutions, Germany)
Dr. Giuseppe Bilotta (Istituto Nazionale di Geofisica e Vulcanologia, Italy)
Dr. Ha Bui (Monash University, Australia)
Prof. Stefano Sibilla (Università di Pavia, Italy)
Prof. Antonio Souto Iglesias (UPM, Spain)
Dr Angelo Tafuni (New Jersey Institute of Technology, US)

Local Organising Committee

Dr Georgios Fourtakas
Dr Steven Lind
Dr Abouzied Nasar
Mr Chunze Cen
Mr Ruofeng Feng
Miss Meixuan Lin
Mr Sumanta Laha

Table of contents

High-performance computing & algorithms

Convergence, consistency and stability

Incompressible flows

Multiple continua and multi-phase flows

Free surface and moving boundaries

Solids and structures

Complex flows I

Artificial intelligence and machine learning

Adaptivity & variable resolution

Boundary conditions

Hydraulic applications

Geotechnical & disaster applications

Process & manufacturing engineering applications

Complex flows II

A way to improve the ghost-particle technique: the clone particles

Matteo Antuono[(a)], Chiara Pilloton[(a)], Andrea Colagrossi[(a),(b)]
& Danilo Durante[(a)]

(*a*) CNR-INM Institute of marine engineering, National Research Council, Rome, Italy
(*b*) Ecole Centrale Nantes, LHEEA research dept. (ECN and CNRS), Nantes, France
andrea.colagrossi@cnr.it

***Abstract*—In the present work we define a novel technique for the enforcement of boundary conditions along solid profiles. Thanks to the absence of interpolation nodes inside the fluid domain associated with the ghost particles, the proposed technique highly simplifies the mirroring procedure described in Marrone et al. [22] without jeopardizing the accuracy and the robustness of the overall approach. The novel technique, called clone particle technique, consists in two main steps. In the first one, the normal and tangent vectors to the solid profile are extended inside the solid body. Then, a local mirroring is applied, meaning that each fluid particle generates its own mirrored field over the solid particles placed inside the body. Unlike Marrone et al. [22], such a mirroring not only applies to the main fluid quantities but also works as a local correction to the normal and tangent fields in the solid body. Such a correction is enforced when the fluid particle is close to sharp profiles, in order to avoid that the fluid particle interacts with the normal vectors along the rear side of the angle/corner. This allows for a straightforward modelling of convex/concave angles and thin solid profiles. Numerical benchmarks at increasing complexity are considered to prove the reliability of the proposed technique. The results are compared and validated with other numerical methods, proving to be accurate and robust.**

I. Introduction

The present work deals with a novel approach for enforcing Solid Boundary Conditions (SBC) along body contours in the Smoothed Particle Hydrodynamics (SPH) scheme. The central importance of a correct SBC implementation pushed the SPHeric community to dedicate the second Grand Challenge of the SPH to this topic (see https://spheric-sph.org/grand-challenges). Several approaches have been presented over the years for both weakly-compressible and incompressible SPH models. Summarizing, these latter can be divided in the following categories:

i) repulsive forces [29, 30],
ii) normal-flux approaches [8, 6],
iii) boundary integrals [16, 21, 28, 12, 18]),
iv) dummy particles [15, 33, 11],
v) ghost particles (also referred to as imaginary particles).

It is well known that approach (i) is rather easy to implement but it suffers of a significant drawback related to the numerical error introduced by the kernel truncation and by the arbitrariness in the choice of the repulsive forces.

A more sound and theoretically-based approach is represented by the normal-flux techniques (ii) which originate in the context of hyperbolic systems of conservation laws.

In the boundary integral technique (iii) the missing area of the kernel support close to the body is taken into account by adding a forcing term to the momentum equation, so that the SBC are satisfied.

As an alternative to the use of wall particles and boundary forces, the dummy particles (iv) represent the first attempt to enforce SBC by filling of the body with solid particles and avoid the errors due to the lack of volume inside the kernel support. In this case, a simple null-velocity field is assigned to the solid particles, while the density field is computed through summation over the neighbouring particles or through interpolation/extrapolation from the fluid.

The ghost-particles approach (v) is already mentioned in [36]. It corresponds to an enhancement of the dummy-particle technique, where a proper ghost-field is assigned to the particles inside the body (hereinafter ghost particles) in order to enforce the required SBC. The ghost particles are placed inside the body by reflecting the positions of the fluid particles during their motion. Both pressure and velocity ghost fields are obtained from the fluid particles through proper mirroring techniques.

The use of ghost particles to enforce velocity and pressure boundary conditions were discussed in [7] for enforcing the boundary conditions in incompressible SPH models. In the latter work the ghost particles have identical properties of real particles while in the former reflective conditions are imposed to simulate a rigid wall. Furthermore, the modelling of both concave and convex right angles with the ghost particles approach is discussed in [17].

The ghost particles approach is easy to implement when the geometry of the boundary has a rectangular (2D) or a cuboid (3D) shape, but difficulties arise when the boundary has a more complex geometry. To overcome this limitation, [22] introduced the Fixed Ghost Particles (FGP), in which the solid particles are fixed in the frame of reference of the solid body. In particular, the field values are obtained through interpolation in correspondence of specific nodes within the fluid domain. These values are then mirrored to the solid particles with specific techniques in such a way that the required SBC are

satisfied (see also [5, 23]). Similar techniques to the FGP of [22] were developed in [1] and, more recently, in [13].

For a thorough comparison between the above-mentioned techniques, we address the reader to the work [32], where the FGP of [22] proved to be one of the most accurate approaches for modelling solid boundaries. Finally, in [26] the FGP was extended to a multi-node technique, allowing for an easier modelling of thin solid boundaries immersed in the fluid.

In two dimensions the FGP permits a reliable treatment of regular solid profiles. However, as underlined in [22], the mirroring procedure around the corners is very complex because of the superimposition or lack of interpolation nodes around the geometric singularities. In those cases the implementation of the FGP technique in a two dimensional framework is not straightforward and its extension to three-dimensional problems may become rather hard. The aim of the present work is, therefore, to overcome those drawbacks with a easier technique without a detriment of accuracy of the FGP approach. To clarify the innovative points with respect to the above-mentioned strategies, we start recalling some details about the mirroring techniques on which the ghost-fluid approach founds.

The idea behind the present work is to extend and simplify the FGP approach presented in [24] by using a local mirroring for both pressure and velocity fields. This is achieved by equipping each fluid particle with a normal and tangential vector fields extrapolated from the solid profile. This technique leads to a global simplification of the algorithm of [24], thanks to the absence of interpolation nodes inside the fluid domain associated with the ghost particles.

The proposed approach is suitable for modelling complex moving bodies with sharp corners and/or geometric singularities. Even the treatment of thin surfaces is naturally embedded and does not require special operations. By getting rid of interpolation nodes within the fluid domain, the generalization of the proposed technique to three dimensions is expected to be easier with respect to the FGP technique. In any case, the extension to three dimensions is not discussed in the present article and it is left to future studies.

Hereinafter, the solid particles with the local mirroring of all the physical quantities are called *clone particles* for distinguishing them from the Fixed Ghost Particles (FGP). The term 'clone' is motivated by the fact that each clone particle takes its mirrored values from a specific fluid particle, instead of relying on a sort of interpolation.

II. Brief recall of the δ^+-SPH scheme

In the present section we summarize the δ^+-SPH scheme, defined in [34] and further inspected in [4], which is the reference model for the simulations shown in the following.

The Navier-Stokes equations for compressible fluids are discretized as a set of fluid particles whose masses m_i are constant during the motion. The particles are initially set on a lattice with homogeneous spacing Δr, and hence the particles' volumes V_i are evaluated initially as Δr^n where n is the number of spatial dimensions. The particle masses m_i are calculated through the initial density field, using the equation of state and the initial pressure field. During the time evolution, volumes V_i change in time according to the particle density ρ_i.

For the sake of brevity, in the following the notation $\boldsymbol{r}_{ji}$ indicates the differences of the particles positions $(\boldsymbol{r}_j - \boldsymbol{r}_i)$ and the same holds for the velocity fields $\boldsymbol{u}_{ji}$ and $\delta\boldsymbol{u}_{ji}$, while for the generic scalar field the notation f_{ij} just indicates the dependency of the field f on the indices i and j.

The spatial gradients are approximated through convolution summations with a kernel function W_{ij}. This function has a compact support whose reference length is denoted by h and referred to as smoothing length. As in [3] a C2-Wendland kernel is adopted in the present work. For this kernel the radius of the support is $2h$ and the number of particles inside the support satisfies the relation $2h = 4\Delta r$. Regarding the spatial derivative of W, due to its properties, it is possible to write $\nabla_i W_{ij} = \boldsymbol{r}_{ji} F_{ij}$, where the scalar function F_{ij} only depends on the particle distance $\|\boldsymbol{r}_{ji}\|$ and it is strictly positive.

The Navier-Stokes equations for compressible fluids are discretized within the δ^+-SPH scheme as:

$$\begin{cases} \dfrac{\mathrm{d}\rho_i}{\mathrm{d}t} &= -\rho_i \displaystyle\sum_j (\boldsymbol{u}_{ji} + \delta\boldsymbol{u}_{ji}) \cdot \nabla_i W_{ij} V_j + \\ & \quad + \displaystyle\sum_j (\rho_j \delta\boldsymbol{u}_j + \rho_i \delta\boldsymbol{u}_i) \cdot \nabla_i W_{ij} V_j + \mathcal{D}_i^\rho \\ \rho_i \dfrac{\mathrm{d}\boldsymbol{u}_i}{\mathrm{d}t} &= \boldsymbol{F}_i^p + \boldsymbol{F}_i^v + \rho_i \boldsymbol{g} + \\ & \quad + \displaystyle\sum_j (\rho_j \boldsymbol{u}_j \otimes \delta\boldsymbol{u}_j + \rho_i \boldsymbol{u}_i \otimes \delta\boldsymbol{u}_i) \cdot \nabla_i W_{ij} V_j \\ \dfrac{\mathrm{d}\boldsymbol{r}_i}{\mathrm{d}t} &= \boldsymbol{u}_i + \delta\boldsymbol{u}_i, \quad V_i = m_i/\rho_i, \quad p = c_0^2(\rho - \rho_0), \end{cases} \tag{1}$$

where $\boldsymbol{F}_i^p$ and $\boldsymbol{F}_i^v$ are the pressure and viscous forces acting on the particle i. The vector $\delta\boldsymbol{u}$ is the Particle Shifting velocity adopted to regularize the particles' spatial distribution during their motion. The specific law for $\delta\boldsymbol{u}$ is described in [27] and is not reported here for the sake of brevity. Incidentally, we highlight that the present shifting technique is based on the use of a shifting velocity rather than a particle displacement, as originally conceived in [19]. Accordingly, the time derivative d/dt used in (1) indicates a quasi-Lagrangian derivative, since the particles are moving with the modified velocity $(\boldsymbol{u} + \delta\boldsymbol{u})$ and the above equations are written in an Arbitrary-Lagrangian-Eulerian framework. For this reason the continuity and the momentum equations contain terms with spatial derivatives of $\delta\boldsymbol{u}$ (for details see [4]).

The term $\mathcal{D}_i^\rho$ is the numerical diffusive term introduced by [2] to filter out the spurious high-frequency noise in the pressure field. Following [3] this term is rewritten as follows:

$$\begin{cases} \mathcal{D}_i^\rho &:= \delta\, c_0\, h \displaystyle\sum_j \psi_{ji} F_{ij} V_j, \\ \psi_{ji} &:= 2\left[(\rho_j - \rho_i) - \dfrac{1}{2}\left(\langle\nabla\rho\rangle_i^L + \langle\nabla\rho\rangle_j^L\right) \cdot \boldsymbol{r}_{ji}\right] \end{cases} \tag{2}$$

where δ is a dimensionless constant set equal to 0.1. The

superscript L in (2) indicates that the gradient is evaluated through the renormalized gradient. Regarding the pressure force $\boldsymbol{F}^p$, following the work by [35] this is expressed as:

$$\begin{cases} \boldsymbol{F}_i^p = -\sum_j \left(p_j + p_i\right) \nabla_i W_{ij} V_j + S_i \sum_j \nabla_i W_{ij} V_j \\ S_i := \begin{cases} 2p_i & \text{for } p_i < 0 \text{ and } i \notin \mathscr{S}_F \\ 0 & \text{elsewhere} \end{cases} \end{cases} \tag{3}$$

where $\mathscr{S}_F$ denotes the region of the fluid domain close to the free surface, that is the free-surface particles and their neighbouring particles. The free-surface particles are detected through the algorithm described in [25].

The last term on the right side of the Eq. (3) leads to a switch in $\boldsymbol{F}_i^p$ from the "plus" formulation of the pressure gradient (namely, $p_j + p_i$) to the minus formulation (that is, $p_j - p_i$) in the fluid regions where the pressure p_i is negative. This switch allows removing the so-called "tensile instability".

For the viscous forces, those are modelled as:

$$\boldsymbol{F}_i^v = \mu \sum_j \frac{(\boldsymbol{u}_j - \boldsymbol{u}_i) \cdot (\boldsymbol{r}_j - \boldsymbol{r}_i)}{\|\boldsymbol{r}_j - \boldsymbol{r}_i\|^2} \nabla_i W_{ij} V_j \tag{4}$$

where μ is the dynamics viscosity.

III. Clone Particles

Before proceeding with the description of the local mirroring of the pressure field, we briefly recall the main steps of the procedure. Apart form some small changes (highlighted in the following), the current technique essentially follows the approach described in [22] for the FGP.

We assume the body profile to be piece-wise regular and we use a spline to discretize it through body nodes equally spaced with distance $\Delta s = \Delta r/4$. Then, the normal and tangent unit vectors are evaluated along the profile, with the normal vectors oriented out of the fluid domain. After that, the body nodes are duplicated out of the fluid domain in the normal direction to create solid particles. This procedure is repeated until the solid body is filled over a kernel radius length (see Fig. 1).

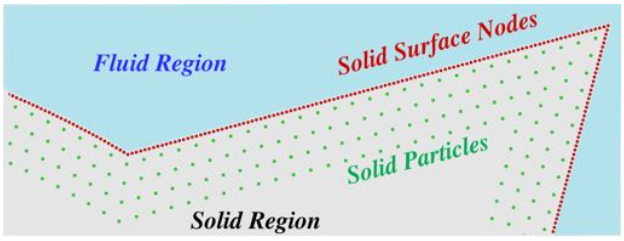

Fig. 1. Sketches of solid surface nodes and solid particles.

After the solid particles are placed, the normal and tangent vectors are extended over them from the body profile. The same is done for the body acceleration, which is assigned as an external condition. In practise, at the end of the procedure each solid particle brings its own acceleration ($\boldsymbol{a}$), normal ($\boldsymbol{n}$) and tangent vectors ($\boldsymbol{\tau}$).

As explained in the next subsection, the fluid particles may locally modify the normal and tangent vectors during their interaction with the solid particles.

A. Local mirroring for the normal and tangent vectors

After the solid particles are generated, a local mirroring procedure is applied. As explained in Section I, this means that each fluid particle generates its own mirrored field over the solid particles. Unlike [22], such a mirroring also applies as a local correction to the normal and tangent fields in the solid body. This correction is needed when the fluid particle is close to sharp corners, in order to avoid that the fluid particle 'sees' the normal vectors to the rear side of the angle/corner. The algorithm is divided in two steps. In the first step, the fluid particle is provided with the normal vector of the closest body node on the body contour (see, for example, Figure 2). The second step consists in a local modification of the normal vectors extended inside the body. By indicating with index i the fluid particle and with j the solid particle in the neighborhood $\mathcal{N}_i$ of the i-th particle, the normal vectors of the j particles remains unchanged if the condition $\boldsymbol{n}_j \cdot (\boldsymbol{r}_j - \boldsymbol{r}_i) \leq 0$ is satisfied by all the solid particles in $\mathcal{N}_i$. On the contrary, if any of the normal vectors $\boldsymbol{n}_j$ satisfies $\boldsymbol{n}_j \cdot (\boldsymbol{r}_j - \boldsymbol{r}_i) > 0$, then $\boldsymbol{n}_j = \boldsymbol{n}_i$ is set for all the j-th solid particles.

Summarizing:

$$\begin{cases} \boldsymbol{n}_j = \boldsymbol{n}_i \quad \forall j \in \mathcal{N}_i \quad \text{if} \quad \max_j \left[\boldsymbol{n}_j \cdot (\boldsymbol{r}_j - \boldsymbol{r}_i) \right] > 0 \\ \boldsymbol{n}_j \quad \text{as mirrored from the solid profile if} \\ \quad \max_j \left[\boldsymbol{n}_j \cdot (\boldsymbol{r}_j - \boldsymbol{r}_i) \right] \leq 0 \end{cases} \tag{5}$$

It is understood that the above change in the normal direction is only valid for the specific particle i under consideration (hence the wording *local mirroring*). The tangent vectors are mirrored accordingly, by assuming that the pair $(\boldsymbol{n}_j, \boldsymbol{\tau}_j)$ forms a right-handed frame of reference.

Figures 3 show some geometrical configurations where the local mirroring is applied.

B. Local mirroring for the velocity and pressure fields

On the basis of the work of [9] and of the theoretical results of [20], different mirroring techniques are used for

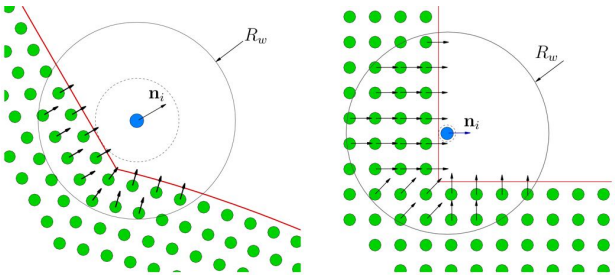

Fig. 2. Sketches of angles where the local modification of the normal vectors (see eq. (5)) does not apply. The fluid particle are in blue while the solid particles are in green. The larger circles represent the kernel support with radius R_W, while the smaller circle indicate the distance from the solid profile.

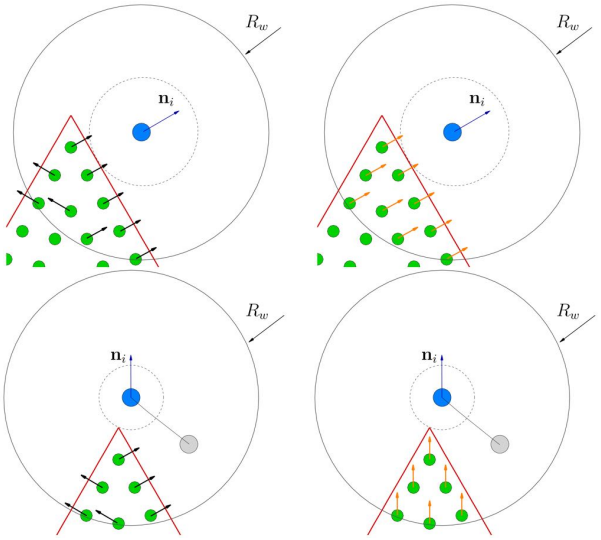

Fig. 3. Sketches of the local mirroring of the normal vectors close to a sharp corner during the motion of a fluid particle around it. In the left column the normal vectors mirrored inside the solid are shown, while in the right column the local mirroring through eq. (5) is displayed. The fluid particles are in blue while the solid particles are in green. The grey particles indicate the previous positions of the fluid particles. The larger circles represent the kernel support with radius R_W, whereas the smaller circles indicate the distance from the solid profile.

the divergence and the Laplacian of the velocity field. This part essentially follows the work of [24]. In particular, for the divergence operator we consider the local mirroring below:

$$\langle \nabla \cdot \boldsymbol{u} \rangle_i : \begin{cases} \boldsymbol{u}_j \cdot \boldsymbol{\tau}_j = \boldsymbol{u}_i \cdot \boldsymbol{\tau}_j \\ \boldsymbol{u}_j \cdot \boldsymbol{n}_j = \left[(\boldsymbol{u}_k^{(b)} - \boldsymbol{u}_i) \dfrac{s_j}{\max(s_i, \Delta s)} + \boldsymbol{u}_k^{(b)} \right] \cdot \boldsymbol{n}_j \end{cases} \tag{6}$$

where the subscripts i and j indicate the quantities associated with the fluid particle i and with its neighboring solid particle j. The velocity $\boldsymbol{u}_k^{(b)}$ is the velocity of the body frontier at the node k, which is the closest to the fluid particle i. Here, s_i and s_j are the distances of the particles i and j from the body contour while Δs is the mean particle distance inside the solid, defined above. The denominator of fraction s_j/s_i is de-singularized such avoiding that a fluid particle approaching to the body contour causes the fraction to diverge. Finally, the mirroring for the Laplacian operator is:

$$\langle \Delta \boldsymbol{u} \rangle_i : \begin{cases} \boldsymbol{u}_j \cdot \boldsymbol{\tau}_j = \left[(\boldsymbol{u}_k^{(b)} - \boldsymbol{u}_i) \dfrac{s_j}{\max(s_i, \Delta s)} + \boldsymbol{u}_k^{(b)} \right] \cdot \boldsymbol{\tau}_j \\ \boldsymbol{u}_j \cdot \boldsymbol{n}_j = \boldsymbol{u}_i \cdot \boldsymbol{n}_j \end{cases} \tag{7}$$

The last step is the definition of a local mirroring for the pressure field, which represents a significant difference respect to [22] where, conversely, the pressure was mirrored through interpolation from the fluid domain. The pressure field at the position of the j-th solid particle is reconstructed by using a Taylor expansion approximation and neglecting the tangential components:

$$p_j \simeq p_i + \left. \frac{\partial p}{\partial n_j} \right|_j (\boldsymbol{r}_j - \boldsymbol{r}_i) \cdot \boldsymbol{n}_j \,. \tag{8}$$

Finally, the component $\partial p/\partial n$ is estimated in analogy to the momentum equation as below:

$$\left. \frac{\partial p}{\partial n_j} \right|_j = \rho \left[\boldsymbol{f}_j - \boldsymbol{a}_j \right] \cdot \boldsymbol{n}_j \,, \tag{9}$$

where $\boldsymbol{f}_j$ is a generic volume force at the j-th position. In equation (9) the viscous term is omitted, since for the Reynolds numbers considered in the present work the effect of the viscosity on the pressure normal gradient is always negligible.

IV. Numerical Validation

In this section we provide some challenging applications where the clone particles are used to model the solid boundaries.

In particular, we consider the flow past a triangular cylinder and an internal flow associated to the roto-translation motion of a spiked cylinder in a confined domain (see Fig. 4). To the authors knowledge the latter was never investigated before and can be useful for the scientific community.

The presence of sharp angles implies the onset of large pressure gradients, which make these test cases particularly challenging. This point was also highlighted in [14], where the flows past a triangular cylinder were simulated with a particle vortex method (named Diffused Vortex Hydrodynamics or DVH) and compared with a Finite Volume Method (FVM). In [14] the simulations were carried out in unbounded domains only, whereas in the present work we consider confined domains. For this reason, the values of the drag and lift coefficients computed in [14] are slightly different than the same results discussed in the present work. Similarly to [14], in the present work an FVM algorithm is also used for comparisons.

The FVM numerical code used in the present work is a thoroughly validated solver named Xnavis and it adopts multi block, body-fitted structured grids that may be eventually overlapped. The solver was developed at INSEAN, the Italian Ship Model Basin (see *e.g.* [31]) and currently used at CNR-INM for researching purposes. Within this solver a Chimera

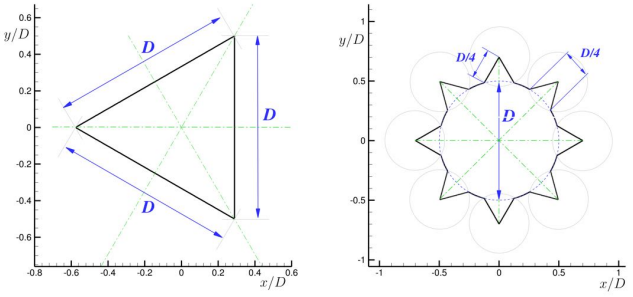

Fig. 4. Sections of the cylinders adopted in the two test-cases.

technique is exploited for managing the dynamic overlapping of different mesh blocks and the matching of the flow fields between different blocks is attained through a body force term included in the momentum equations. The mesh stretching toward the body wall guarantees that the first cells' line over the body has a height $\Delta h \ll y^+$. In the boundary layer region the spatial resolution of the FVM is always finer than the SPH.

1) Viscous Flow past a triangular Cylinder at Re = 1000: In the present Section the flow past a triangular cylinder is investigated. For this test case the accuracy of the clone particles technique for describing the body walls is crucial because of the presence of sharp angles. The centroids of the cylinders are placed at the origin of the reference frame and the fluid domain spans $[-6D, 12D]\times[-4D, 4D]$ where D is the side of the triangle. An inflow boundary condition is enforced on the left side of the domain (*i.e.* $x = -6D$), while an outflow condition is implemented on the right side ($x = 12D$). Finally, on the horizontal planes at $y = \pm 4D$ free-slip conditions are enforced. A free stream of constant intensity U along the x-axis is considered whereas the speed of sound is set equal to $c_0 = 10U$. The Reynolds number is defined as $\mathrm{Re} = \rho U D/\mu$, Re = 1000 are considered for the simulations. In order to avoid an impulsive start, the inflow velocity U is reached through an acceleration ramp, as described below:

$$u(t) = U \begin{cases} \tau^2(3 - 2\tau), & \tau < 1; \\ 1, & \tau \geq 1, \end{cases}$$

with $\tau = t\,U/D$. We underline that the use of the time-ramp for the flow rate avoids the onset of pressure shock waves, and their consequent reflections, due to the impulsive start.

According the definitions above, the drag, lift, torque coefficients and the Strouhal number are defined as:

$$C_D = \frac{F_x}{\frac{1}{2}\rho U^2 D L}, \quad C_L = \frac{F_y}{\frac{1}{2}\rho U^2 D L}$$
$$C_M = \frac{M_z}{\frac{1}{2}\rho U^2 D^2 L}, \quad \mathrm{St} = \frac{f D}{U} \qquad (10)$$

where f denotes the frequency of the vortex shedding. For the sake of clearness, hereinafter the symbol $N = D/\Delta r$ indicates the spatial resolution of the simulations.

Details of the flow fields near the cylinder are shown in figure 5. In the right panel a snapshots of the pressure field is provided, with the aim of highlighting the large gradients that occur on the rear side of the cylinder.

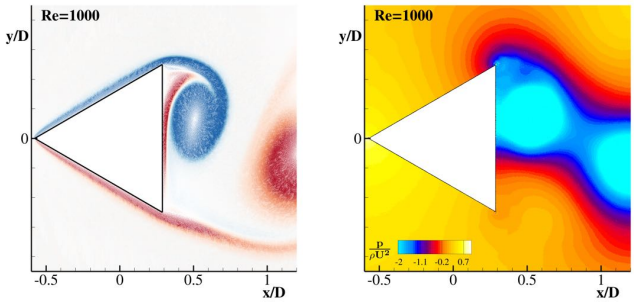

Fig. 5. Triangular cylinder. Vorticity (left) and pressure (right) fields at maximum lift force for Re = 1000. Vorticity color map range from -10 to 10.

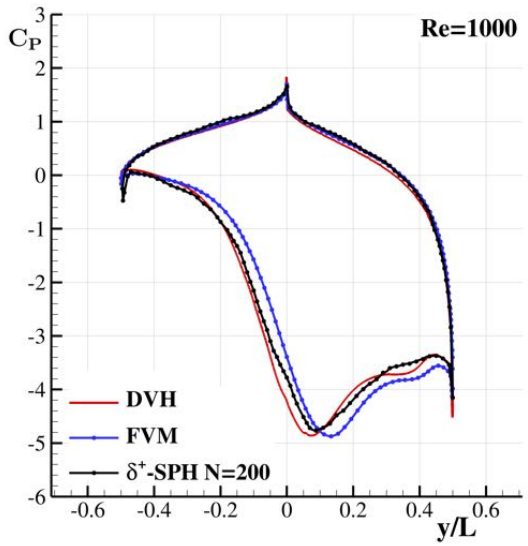

Fig. 6. Triangular cylinder. Pressure coefficient evaluated along the body contour for maximum lift. Comparison between the FVM, the DVH and the δ^+-SPH solver for Re = 1000 (right).

	C_D	C_L	C_M	St
$N = 50$	3.05 ± 0.455	±0.721	±0.464	0.191
$N = 100$	2.87 ± 0.475	±0.709	±0.400	0.199
$N = 200$	2.73 ± 0.402	±0.700	±0.349	0.210
FVM	2.33 ± 0.330	±0.650	±0.355	0.213

TABLE I
FORCE COEFFICIENTS (MEAN ± OSCILLATION AMPLITUDE) FOR TRIANGULAR CYLINDER AT RE = 1000.

The presence of high gradients is further highlighted in figure 6 where the pressure coefficient C_p is computed along the contour of the body at maximum lift force. The solution of δ^+-SPH solver is compared with the outputs of the FVM code and of the DVH method, described in [14]. The results of the δ^+-SPH scheme are between the FVM and the DVH and exhibit a good agreement with the other solvers for both the Reynolds numbers. The accuracy of the clone particle approach is further confirmed in Table I where the coefficients C_D, C_L, C_p and the Strouhal number St are computed with different spatial resolutions. Again, a good agreement with the FVM outputs is achieved.

A. Flow generated by roto-traslating spiked circular cylinder in a confined domain at Re = 100 and Re = 1000

The last and challenging benchmark is the roto-translating motion of a spiked cylinder in a confined domain. In this case, the centre of the cylinder is placed at the origin of the reference frame and the fluid domain is a solid box with dimensions $[-3D, 11D] \times [-3D, 3D]$. Free-slip boundary conditions are enforced on the domain walls, whereas no-slip conditions are imposed on the cylinder contour.

Figure 7 shows the time laws of the horizontal displacement

of the centroid $x_G(t)$ and of the angle of rotation $\theta_G(t)$ around the centroid. The time laws are composed by piecewise functions composed by constant acceleration stages followed by constant velocity motions. Here U indicates the maximum horizontal velocity reached by the centroid, and it is used as reference in the definition of the Reynolds number, *i.e.* $\mathrm{Re} = U\,D/\nu$.

The dynamic Chimera approach used in the FVM code Xnavis is able to manage the overlapping of the near body-fitted mesh on the background fixed mesh. In order to correctly describe the vorticity evolution within the domain box, such avoiding a severe numerical diffusion, a sufficiently mesh with high resolution is adopted. The total number of numerical volumes exceeds 1.5 Mln.

Figure 8 shows four time instants of the evolution of the vorticity field for Re = 100. The left column contains the results from the FVM, while the right column the outputs of the δ^+-SPH . It can be appreciated that, despite the complexity of the body contour, the vorticity fields are very similar at this Reynolds number. The thin vortex structures shed by the cylinder and stretched by its motion are well captured by both codes and a remarkable agreement can be appreciated. Some minor discrepancies are appreciable at the final simulation instant, however not affecting the overall quality of the comparison.

The time history of the forces confirms what highlighted by comparison of the vorticity fields. Although the drag coefficient calculated with δ^+-SPH is more oscillating, the match between the two approaches is very encouraging. In particular, despite its small variation range, the torque C_M is the coefficient that is more affected by the fluid-body interaction for a roto-translating body and the superposition between the two outcomes is remarkable.

At higher Reynolds numbers, the situation becomes more critical and even little local discrepancies may amplify the global disagreement between results. In figure 9, the same time instants depicted in figure 8 are proposed again. At $t\,U/D = 5$ and $t\,U/D = 10$ a good agreement is obtained, whereas for later times a significant departure between the δ^+-SPH and FVM solutions is evident. Small differences in the shed vorticity are amplified with time, leading to different final configurations of the dipoles within the fluid domain.

Despite this, the force coefficients are in a fairly good agreement, as depicted in the right column of figure 10. The

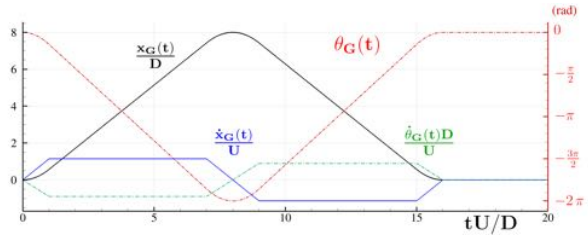

Fig. 7. Time law for the motion imposed to the spiked circular cylinder. Solid lines represent the displacement $x_G(t)$ and velocity $\dot{x}_G(t)$ of the centroid, while the dashed-dotted line refers to the angle of rotation $\theta_G(t)$ and to the angular velocity $\dot{\theta}_G$ around the centroid.

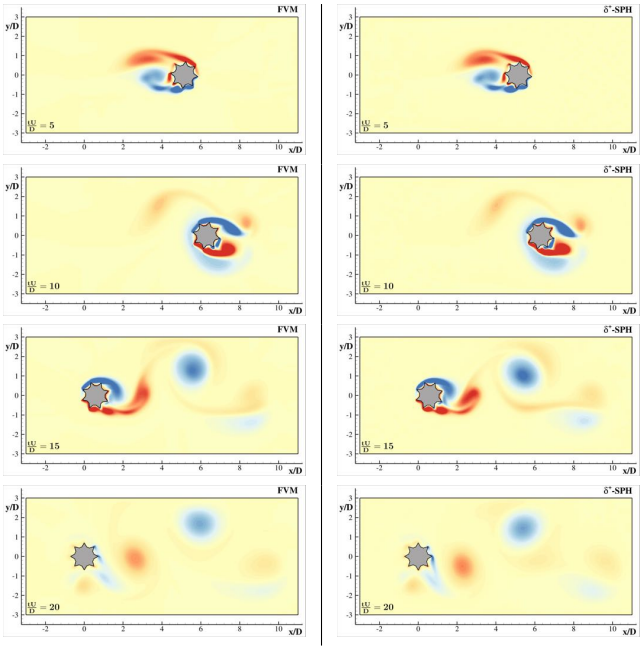

Fig. 8. Flow generated by the roto-translating spiked circular cylinder in a confined domain at Re = 100. Vorticity fields by FVM (left columns) and by δ^+-SPH (right column). The color map range from -5 to 5. The full video of the δ^+-SPH simulation is available at Link Video N1.

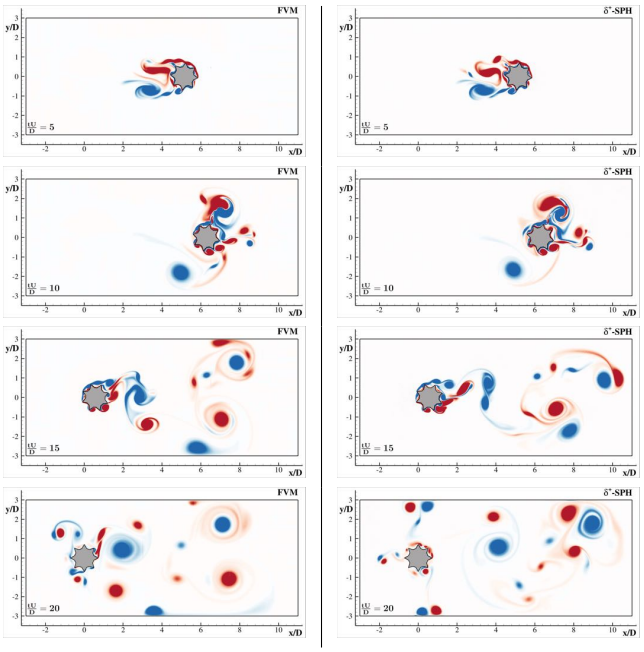

Fig. 9. Flow generated by the roto-translating spiked circular cylinder in a confined domain at Re = 1000. Vorticity fields by FVM (left columns) and by δ^+-SPH (right column). The color map range from -10 to 10. The full video of the δ^+-SPH simulation is available at Link Video N2.

presence of little vorticity scales in the domain induces high frequency oscillations of the forces on the body, but the global behaviour is rather similar between the two codes. The lift coefficient, which is less oscillating than the drag (see also [10]), shows a remarkable superposition between the results in particular when the cylinder inverts its motion and a large

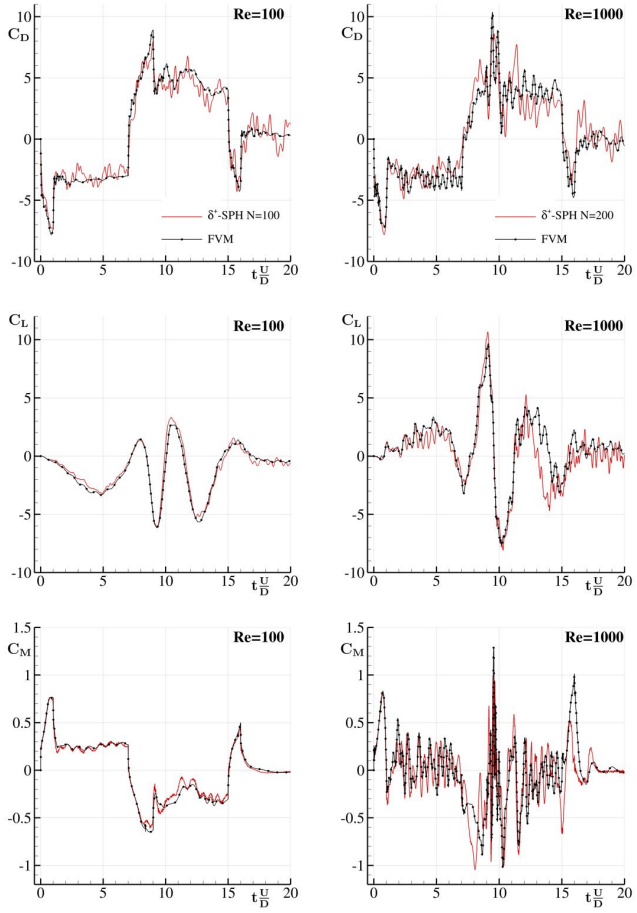

Fig. 10. Force coefficients from the roto-translating spiked circular cylinder in a confined domain at Re = 100 (left column) and Re = 1000 (right column), obtained using the FVM (black dot-solid lines) and the δ^+-SPH (red solid lines).

oscillation is exhibited.

V. Conclusions

In the present work we proposed a new technique for the enforcement of boundary conditions along solid profiles, which highly simplifies the mirroring procedure described in [22], without jeopardizing the accuracy and the robustness of the overall approach. The clone particles algorithm is based on a local mirroring of the flow fields after the local definition of the normal and tangent vectors over the solid body.

The proposed technique is tested on benchmarks of increasing complexity and compared with a Finite Volume Method and a vortex particle method (the DVH described in [14]), proving to be accurate and robust.

The present work is restricted to the analysis of two-dimensional problems, although, in principle, the proposed algorithm can be extended to three-dimensions without any substantial change. This topic, which is currently under investigation, will be considered in future studies, especially for applications with complex fluid-structure interactions. Similarly, the proposed technique will be adopted in the analysis of free-surface and multi-phase flows.

Acknowledgments

The research was developed within the Project Area Applied Mathematics of the Department of Engineering, ICT and Technology for Energy and Transport (DIITET) of the Italian National Research Council (CNR). This work was performed by using HPC resources of the Centrale Nantes Supercomputing Centre on the cluster Liger.

References

[1] S. Adami, X. Y. Hu, and N. A. Adams. A generalized wall boundary condition for smoothed particle hydrodynamics. *Journal of Computational Physics*, 231(21):7057–7075, 2012.

[2] M. Antuono, A. Colagrossi, and S. Marrone. Numerical diffusive terms in weakly-compressible SPH schemes. *Computer Physics Communications*, 183(12):2570–2580, 2012.

[3] M. Antuono, S. Marrone, A. Di Mascio, and A. Colagrossi. Smoothed particle hydrodynamics method from a large eddy simulation perspective. generalization to a quasi-lagrangian model. *Physics of Fluids*, 33(1):015102, 2021.

[4] M. Antuono, P.N. Sun, S. Marrone, and A. Colagrossi. The δ-ALE-SPH model: An arbitrary lagrangian-eulerian framework for the δ-SPH model with particle shifting technique. *Computers & Fluids*, 216:104806, 2021.

[5] B Bouscasse, A Colagrossi, S Marrone, and M Antuono. Nonlinear water wave interaction with floating bodies in sph. *Journal of Fluids and Structures*, 42:112–129, 2013.

[6] L. Chiron, M. De Leffe, G. Oger, and D. Le Touzé. Fast and accurate sph modelling of 3d complex wall boundaries in viscous and non viscous flows. *Computer Physics Communications*, 234:93–111, 2019.

[7] S. J. Cummins and M. Rudman. An sph projection method. *Journal of computational physics*, 152(2):584–607, 1999.

[8] M. De Leffe, D. Le Touzé, and B. Alessandrini. Normal flux method at the boundary for SPH. In 4^{th} *SPHERIC*, pages 149–156, May 2009.

[9] M. De Leffe, D. Le Touzé, and B. Alessandrini. A modified no-slip condition in weakly-compressible SPH. In *6th ERCOFTAC SPHERIC workshop on SPH applications*, pages 291–297, 2011.

[10] D. Durante, E. Rossi, and A. Colagrossi. Bifurcations and chaos transition of the flow over an airfoil at low reynolds number varying the angle of attack. *Communications in Nonlinear Science and Numerical Simulation*, 89:105285, 2020.

[11] A. English, JM Domínguez, R. Vacondio, AJC Crespo, PK Stansby, SJ Lind, L. Chiapponi, and M Gómez-Gesteira. Modified dynamic boundary conditions (mdbc) for general-purpose smoothed particle hydrodynamics (sph): Application to tank sloshing, dam break and

fish pass problems. *Computational Particle Mechanics*, 9(5):1–15, 2022.

[12] M. Ferrand, D. R. Laurence, B. D. Rogers, D. Violeau, and C. Kassiotis. Unified semi-analytical wall boundary conditions for inviscid, laminar or turbulent flows in the meshless SPH method. *International Journal for Numerical Methods in Fluids*, 71(4):446–472, 2013.

[13] G. Fourtakas, J. M. Dominguez, R. Vacondio, and B. D. Rogers. Local uniform stencil (lust) boundary condition for arbitrary 3-d boundaries in parallel smoothed particle hydrodynamics (sph) models. *Computers & Fluids*, 190:346–361, 2019.

[14] O Giannopoulou, A Colagrossi, A Di Mascio, and C Mascia. Chorin's approaches revisited: vortex particle method vs finite volume method. *Engineering Analysis with Boundary Elements*, 106:371–388, 2019.

[15] S. Koshizuka, A. Nobe, and Y. Oka. Numerical analysis of breaking waves using the moving particle semi-implicit method. *International Journal for Numerical Methods in Fluids*, 26(7):751–769, 1998.

[16] S. Kulasegaram, J. Bonet, RW Lewis, and M. Profit. A variational formulation based contact algorithm for rigid boundaries in two-dimensional sph applications. *Computational Mechanics*, 33(4):316–325, 2004.

[17] E. S Lee, C. Moulinec, R. Xu, D. Violeau, D. Laurence, and P. Stansby. Comparisons of weakly compressible and truly incompressible algorithms for the SPH mesh free particle method. *Journal of Computational Physics*, 227(18):8417–8436, 9/10 2008.

[18] A. Leroy, D. Violeau, M. Ferrand, and C. Kassiotis. Unified semi-analytical wall boundary conditions applied to 2-d incompressible sph. *Journal of Computational Physics*, 261:106–129, 2014.

[19] S.J. Lind, R. Xu, P.K. Stansby, and B.D. Rogers. Incompressible smoothed particle hydrodynamics for free-surface flows: A generalised diffusion-based algorithm for stability and validations for impulsive flows and propagating waves. *Journal of Computational Physics*, 231(4):1499–1523, 2012.

[20] F. Macià, M. Antuono, L. M. González, and A. Colagrossi. Theoretical Analysis of the No-Slip Boundary Condition Enforcement in SPH Methods. *Progress of Theoretical Physics*, 125(6):1091–1121, 2011.

[21] J.-C. Marongiu, F. Leboeuf, J. Caro, and E. Parkinson. Free surface flows simulations in Pelton turbines using an hybrid SPH-ALE method. *Journal of Hydraulic Research*, 48(S1):40–49, 2010.

[22] S. Marrone, M. Antuono, A. Colagrossi, G. Colicchio, D. Le Touzé, and G. Graziani. Delta-SPH model for simulating violent impact flows. *Computer Methods in Applied Mechanics and Engineering*, 200(13-16):1526–1542, 2011.

[23] S. Marrone, A. Colagrossi, M. Antuono, G. Colicchio, and G. Graziani. An accurate sph modeling of viscous flows around bodies at low and moderate reynolds numbers. *Journal of Computational Physics*, 245:456–475, 2013.

[24] S. Marrone, A. Colagrossi, M. Antuono, G. Colicchio, and G. Graziani. An accurate SPH modeling of viscous flows around bodies at low and moderate Reynolds numbers. *Journal of Computational Physics*, 245:456–475, 2013.

[25] S. Marrone, A. Colagrossi, D. Le Touzé, and G. Graziani. Fast free-surface detection and level-set function definition in SPH solvers. *Journal of Computational Physics*, 229(10):3652–3663, 2010.

[26] D. D. Meringolo, F. Aristodemo, and P. Veltri. SPH numerical modeling of wave–perforated breakwater interaction. *Coastal Engineering*, 101:48–68, 2015.

[27] J Michel, D Durante, A Colagrossi, and S Marrone. Energy dissipation in violent three-dimensional sloshing flows induced by high-frequency vertical accelerations. *Physics of Fluids*, 34(10):102114, 2022.

[28] A. D. Monaco, S. Manenti, M. Gallati, S. Sibilla, G. Agate, and R. Guandalini. Sph modeling of solid boundaries through a semi-analytic approach. *Engineering Applications of Computational Fluid Mechanics*, 5(1):1–15, 2011.

[29] J.J. Monaghan. Simulating Free Surface Flows with SPH. *J. Comp. Phys.*, 110(2):39–406, 1994.

[30] J.J. Monaghan and J.B. Kajtar. SPH particle boundary forces for arbitrary boundaries. *Computer Physics Communications*, 180(10):1811–1820, 2009.

[31] R Muscari, R Broglia, and A Di Mascio. An overlapping grids approach for moving bodies problems. In *The Sixteenth International Offshore and Polar Engineering Conference*. OnePetro, 2006.

[32] Pawan Negi and Prabhu Ramachandran. How to train your solver: Verification of boundary conditions for smoothed particle hydrodynamics. *Physics of Fluids*, In Press, 2022.

[33] S. Shao and E.Y.M. Lo. Incompressible SPH method for simulating Newtonian and non-Newtonian flows with a free surface. *Advances in Water Resources*, 26(7):787–800, 2003.

[34] P.N. Sun, A. Colagrossi, S. Marrone, M. Antuono, and A.-M. Zhang. A consistent approach to particle shifting in the δ-Plus-SPH model. *Computer Methods in Applied Mechanics and Engineering*, 348:912–934, 2019.

[35] P.N. Sun, A. Colagrossi, S. Marrone, M. Antuono, and A.M. Zhang. Multi-resolution Delta-plus-SPH with tensile instability control: Towards high reynolds number flows. *Computer Physics Communications*, 224:63–80, 2018.

[36] J.P. Vila. On particle weighted methods and Smooth Particle Hydrodynamics. *Mathematical Models & Methods in Applied Sciences*, 9(2):161–209, 1999.